Fundamental Study of Hybrid Wind Tunnel Integrating Numerical Simulation and Experiment in Analysis of Flow Field*

Keisuke NISUGI**, Toshiyuki HAYASE*** and Atsushi SHIRAI***

This paper deals with a new flow analysis system, namely *the hybrid wind tunnel*, which integrates the experimental measurement with a wind tunnel and a corresponding numerical simulation with a computer. Analysis here is performed for the fundamental flow with the Karman vortex street in a wake of a square cylinder. A specific feature of the hybrid wind tunnel is existence of the feedback signal to compensate the error in the pressure on the side walls of the cylinder and the feed-forward signal to adjust the upstream velocity boundary condition. Investigation is focused on evaluating the hybrid wind tunnel as a flow analysis methodology with respect to the ordinary simulation and the experiment. As compared with the ordinary simulation, the hybrid wind tunnel substantially improves the accuracy and the efficiency in the analysis of the flow. Especially, the oscillation of the flow due to the Karman vortex street reproduced with the hybrid wind tunnel exactly synchronizes with that of the experiment, while that with the ordinary simulation never behave like that. In comparison with the experiment, the hybrid wind tunnel provides more detailed information of the flow than the experiment does.

Key Words: Hybrid Wind Tunnel, Numerical Analysis, Experiment, Integration, Flow Observer, Numerical Realization, Karman Vortex Street

1. Introduction

Experiment and numerical simulation are essential tools in analysis of flow problems. Each of these, however, has both advantages and disadvantages. In experiment, the reliability of the result is easy to evaluate, but detailed information of the whole flow field, such as the velocity vector field or the pressure field, is difficult to obtain. Numerical simulation, on the other hand, easily yields any information of the flow field. However, the reliability of the result strongly depends on the numerical model, and, especially in analysis of the real flows, the numerical solution represents not necessarily the exact flow field but the one with identical statistics to the relevant flow due to the lack of the exact boundary condition and/or the initial condition.

Hayase et al.[1] proposed an analysis methodology for flow problems, namely the flow observer, which integrates an experimental measurement and a numerical simulation (Fig. 1). The flow observer is conceptually the state observer in control theory applied to the flow analysis. For a real flow to be investigated, the simulation model is constructed in a computer through a standard numerical analysis methodology based on the fundamental equations with appropriate boundary and initial conditions. Some output signals are defined for the real flow measurement and for the numerical simulation in order to evaluate the difference between both the results. Numerical simulation is carried out with the additional body force or the boundary condition as the feedback signal that is derived from the difference between the both output signals. If the feedback law is designed properly, the computational result converges to the real flow. The flow observer is expected to eventually yield complete information of the real flow through the numerical simulation with limited information at a finite number of measurement points. In the former work, numerical simulation of the flow observer was performed for the turbulent flow through a square duct. The turbulent flow structure including fluctuation was successfully reproduced by the feedback of axial velocity components at 100 points on a cross section. However, validity

* Received 3rd June, 2003 (No. 03-4094)

** Graduate School of Information Science, Tohoku University, 2–1–1 Katahira, Aoba-ku, Sendai, Miyagi 980–8577, Japan

*** Institute of Fluid Science, Tohoku University, 2–1–1 Katahira, Aoba-ku, Sendai, Miyagi 980–8577, Japan. E-mail: hayase@ifs.tohoku.ac.jp

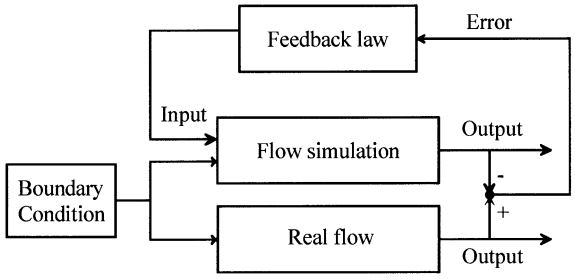

Fig. 1 Structure of the flow observer

of the flow observer has not been confirmed in a real flow system.

As a fundamental flow of theoretical and practical importances, many studies have been carried out on the Karman vortex street behind a square cylinder. For example, Lee[2] investigated the effect of turbulence by measuring the pressure distribution on the cylinder surface, and Lyn et al.[3] measured the unsteady velocity field around the cylinder by Laser-Doppler-Velocimetry (LDV). Rodi et al.[4] summarized several numerical studies, pointing out that computational results for the drag, the Strouhal number, and the velocity distributions are strongly influenced by the number of grid points, the discretization method, and the boundary condition treatment. Because of the reason mentioned above, it is difficult to exactly reproduce the structure of the Karman vortex street in a real flow with either the experiment or the numerical simulation.

Flow control is a typical issue that requires the exact representation of real flows in real-time. Recently, many researchers have concerned the control problem of the Karman vortex street, such as the passive control by inserting a second rod[5], or the open-loop control by oscillating the cylinder[6]. As the feedback control, Roussopoulos[7] successfully suppressed the vortex shedding by actuating speakers in accordance with the velocity measurement by a hot wire anemometer in the wake. Although feedback control is usually very effective, it sometimes encounters difficulties in practical applications; for example, the sensor sometimes disturbs the flow field, or the measurable information of the flow is limited near the object. A possible solution for the problem is the flow observer that reproduces any state variable in the flow domain from measurable variables, such as pressure on the cylinder surface.

In this study, for the flow with the Karman vortex street in a wake behind a square cylinder, the hybrid wind tunnel is developed by integrating the experimental measurement with a wind tunnel and a corresponding numerical simulation with a computer in the framework of the flow observer. Usefulness of the hybrid wind tunnel is investigated by comparing the results with those of the experiment and the ordinary simulation. Section 2 of the paper explains the experimental measurement with a wind tunnel and the numerical simulation method, and describes how they are integrated into the hybrid wind tunnel. In section 3, the feedback and the feed forward parameters are determined based on the velocity at the monitoring point in the wake. The sensitivity of the analysis to the parameters is also investigated. The reproducibility of the whole flow field is evaluated in comparison among the hybrid wind tunnel, the LDV measurement, and the ordinary simulation. Since this paper focuses on the accuracy of the hybrid wind tunnel, the analysis is performed as off-line process and realization of real-time analysis is set aside. Section 4 summarizes the conclusions of this work.

Nomenclature

A_c : cross-sectional area of the control volume
D : width of square cylinder
$\boldsymbol{f}$: body force
f_A, f_B : artificial forces to x-directional control volumes A′ and B′, respectively (Fig. 3)
h_t : time increment
h_x, h_y : computational grid spacings in x and y directions, respectively
K : proportional feedback gain
K_e : velocity coefficient
L_x, L_y : lengths of computational domain in x and y directions, respectively
N_x, N_y : numbers of grid points in x and y directions, respectively
P_m : dynamic pressure
Re : $= DU_0/\nu$, Reynolds number
T : time
T_c : time constant of low-pass filter
$\boldsymbol{u}$: $= (u,v,w)$, velocity vector in Cartesian coordinate system (x,y,z)
U_b : upstream boundary velocity in calculation
U_e : estimation of U_0
U_0 : upstream uniform flow velocity in experiment
u' : perturbation of velocity u
(x,y,z) : Cartesian coordinate system
ρ : density of fluid
ν : kinematic viscosity

Superscript

$*$: experimental value

Subscript

rms : root mean square value
mean : mean value averaged in time

2. Structure of the Hybrid Wind Tunnel

The hybrid wind tunnel consists of an experimental measurement with a wind tunnel and a corresponding numerical simulation with a computer. In this section these components are first explained, along with their integration into the hybrid wind tunnel.

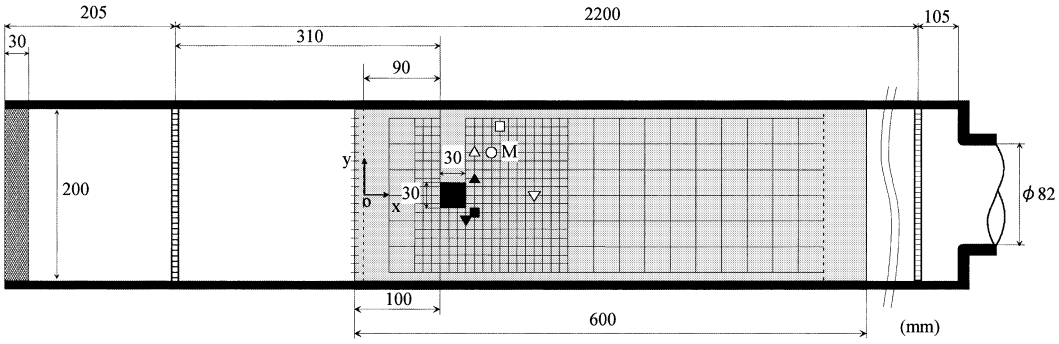

Fig. 2 Geometry of the experimental system. Grid points represent LDV measurement points. Symbol ∘ denotes the monitoring point **M** of the velocity u to determine the parameters of the hybrid wind tunnel. Other symbols represent points where the hybrid wind tunnel results in maximum error (open symbols) or minimum error (closed ones) for the mean velocity u_{mean}(▽,▼), the rms of the velocity perturbation u'_{rms}(□,■), and rms error in the velocity u(△,▲).

2.1 Wind tunnel experiment

Figure 2 illustrates the geometry of the wind tunnel experiment. The wind tunnel measures 2 510 mm in length and 200 × 200 mm in cross section. The downstream (right) end of the tunnel is connected to a blower (Nishimura, NK-200) via a flexible tube measuring 3 m in length and 82 mm in diameter. The suction flow of the blower is controlled by an inverter (MITSUBISHI, FR-E520-1.5 K). As a flow-straightening device, a filter (Bridgestone, Everlight SR HR-13, 30 mm in thickness) is placed at the upstream end of the tunnel, and steel mesh plates (5 mm mesh size, 1 mm in thickness) are set at 205 mm (upstream side) and 105 mm (downstream side) inward from the respective ends of the tunnel. The square cylinder (acrylic, 30 × 30 × 200 mm) is placed 310 mm downstream from the upstream steel mesh plate, at the center of the tunnel width. The Cartesian coordinate system (x,y,z) is defined as shown in the figure.

For the experimental condition, the upstream uniform flow velocity U_0, averaged over a 180 × 180 mm region on a cross-section at $x = 0$ to avoid the boundary layer effect, is set to 0.6 m/s with a Reynolds number Re $(= U_0 D/\nu)$ of 1 200. Non-uniformity of the mean velocity distribution on this section is 3.5%. Under this condition a Karman vortex street with shedding frequency of 2.75 Hz was observed.

The details of the square cylinder are illustrated in the upper left side of Fig. 3. Pressure holes are provided at the center of the front and side walls. They are connected to differential pressure transducers (SSK, DP8A-2) via copper tubes of 3 mm inner diameter and 200 mm length, and vinyl tubes of 8 mm inner diameter and 200 mm length. The differential pressure between the center of each side wall and that of the front wall is measured. High-frequency noise of the pressure signals is removed through a low-pass filter with a cut-off frequency of 10 Hz, in consideration of the shedding frequency of the

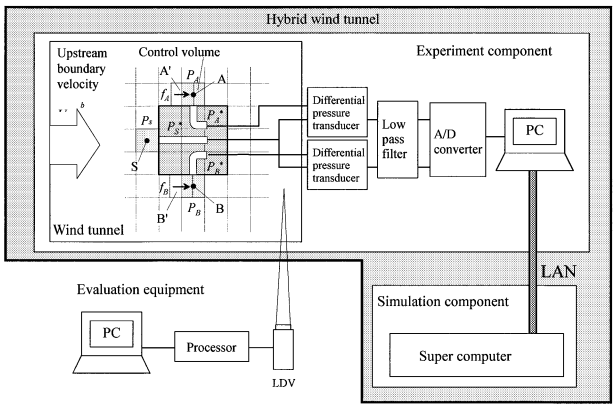

Fig. 3 Construction of the experimental system and definition of the output, feedback, and feed-forward signals

Karman vortex (2.75 Hz). The pressure signals are then input to the PC via an A/D converter at a sampling frequency of 1 000 Hz. Note that a sufficiently large sampling frequency is specified in considering future work in the turbulent flow regime. The measured pressure signals are transmitted to the computer (SGI, Origin 2 000, 300 MHz, 1 CPU) via a high-speed network as shown in the bottom right part of Fig. 3. Details of the numerical simulation using the measurement signals are explained in the next section.

The bottom left side of Fig. 3 illustrates the equipment to evaluate the hybrid wind tunnel. The velocity component u was measured with the Laser Doppler Velocimetry (TSI, LDP100). The 413 measurement points, the nodal points of the grid on the middle plane $(z = 0)$ as shown in Fig. 2, are concentrated with an interval of 10 mm near the cylinder, whereas the other points rather sparsely distributed with intervals of 30 mm. Oil mist (average diameter of 1 μm) is supplied to the wind tunnel by a fog generator (DANTEC, 2010). The number of valid data obtained in LDV processing is about 500 samples per sec-

ond. Pressure and velocity were measured for 30 seconds at each measurement point.

2.2 Numerical simulation

In the numerical simulation, we ignore the three-dimensional effect of the flow, focusing on the primary two-dimensional structure of the Karman vortex street. The two-dimensional domain of $L_x \times L_y = 20D \times 7D$ is defined as the shaded region in Fig. 2.

Governing equations for incompressible and viscous fluid flow consist of the Navier-Stokes equation

$$\rho\left(\frac{\partial \boldsymbol{u}}{\partial t} + (\boldsymbol{u}\cdot\mathrm{grad})\boldsymbol{u}\right) = -\mathrm{grad}P + \mu\nabla^2\boldsymbol{u} + \boldsymbol{f}, \qquad (1)$$

and the equation of continuity

$$\mathrm{div}\boldsymbol{u} = 0, \qquad (2)$$

where $\boldsymbol{f}$ in Eq. (1) is the body force term corresponding to the feedback signal in the hybrid wind tunnel (physical meaning of this additional term is discussed in section 2.3).

As the boundary condition, parallel flow with uniform velocity U_b is applied at the upstream boundary,

$$u(y) = U_b,\ v(y) = 0 \text{ at } x = -10\,\mathrm{mm}, \qquad (3)$$

where the upstream boundary velocity U_b is treated as the feed-forward signal in the hybrid wind tunnel. The downstream boundary condition is free stream. The no-slip condition is applied on the solid walls. All velocity components of the flow field are initially set null.

A uniformly spaced staggered grid system of $N_x \times N_y = 60 \times 21$ with grid spacing of 10 mm ($D/3$) is defined in the computational domain. The governing equations discretized with the finite volume method are solved with the SIMPLER[8]-based method. In this numerical methodology, a consistently reformulated QUICK scheme is applied to the convective terms[9], and the second order implicit scheme to the time derivative terms[10]. A rather coarse grid system is adopted in the hybrid wind tunnel, in expectation of improved grid-convergence property due to inclusion of the experimental data[1], and in consideration of the reduction in the computational load for future real-time operation (although off-line analysis is performed in the present paper). Because of the uniform grid spacing, the width of the channel for computation ($7D = 210$ mm) is 5% wider than that of the experiment (200 mm). It is noted that this difference causes local reduction of the mean flow velocity between the cylinder and the sidewall by 5.6%, possibly resulting in reduction in the oscillation frequency of the same order. Sufficiently small time step of 1 ms identical to the sampling time of the pressure measurement is used in the calculation. Table 1 summarizes the condition of the hybrid wind tunnel used in this study.

2.3 Integration method of measurement and simulation

Integration of the experimental measurement and the numerical simulation in the hybrid wind tunnel is explained here. Since the vortex shedding in the wake reflects on the pressure on both sides of the cylinder, we define the output signals as the differential pressure between the center of each side wall and that of the front wall of the cylinder as,

Table 1 Conditions of hybrid wind tunnel

Square cylinder width	D	0.03 m
Mean velocity	U_0	0.605 m/s
Density of air [20°C]	ρ	1.229 kg/m^3
Reynolds number	R_e	1200
Computational domain	$L_x \times L_y$	$20D \times 7D$
Grid points	$N_x \times N_y$	60×21
Grid spacing	$h_x \times h_y$	$D/3 \times D/3$
Time step	h_t	0.001 s
CPU time for one time step		0.18 s

Experiment:

$$\begin{pmatrix} P^*_{AS} \\ P^*_{BS} \end{pmatrix} = \begin{pmatrix} P^*_A - P^*_S \\ P^*_B - P^*_S \end{pmatrix}. \qquad (4)$$

Numerical simulation:

$$\begin{pmatrix} P_{AS} \\ P_{BS} \end{pmatrix} = \begin{pmatrix} P_A - P_S \\ P_B - P_S \end{pmatrix}, \qquad (5)$$

where P_A, P_B, and P_S are pressures at the control volumes A, B, and S, respectively (see Fig. 3).

The body force $\boldsymbol{f}$ in Eq. (1) is determined to be proportional to the difference between these output signals, and applied to the numerical simulation as the feedback signal of the hybrid wind tunnel,

$$\begin{pmatrix} f_A \\ f_B \end{pmatrix} = -KA_C \begin{pmatrix} P_{AS} - P_{AS}{}^* \\ P_{BS} - P_{BS}{}^* \end{pmatrix}, \qquad (6)$$

where f_A and f_B represent the artificial force in the x-directional momentum equation in the control volumes A′ and B′ (dashed boxes in Fig. 3), respectively, K the feedback gain, and A_c the cross-sectional area of the control volume. The velocity component u is accelerated or decelerated by the feedback of Eq. (6) at the upstream boundary of the pressure control volume A or B. As a result, the pressure error in the pressure equation reduces in these control volumes.

Physical meaning of the feedback signal is discussed here. If the numerical simulation correctly solves the Navier-Stokes equation and the equation of continuity with respect to the boundary and initial conditions, the additional body force $\boldsymbol{f}$ in Eq. (1) should be zero. However, numerical simulation is generally incapable to exactly reproduce real flows due to the following reasons:

(1) Unknown initial condition
(2) Unknown or incorrect boundary condition
(3) Existence of unknown disturbance
(4) Inappropriate assumptions (such as two-dimensionality)
(5) Numerical error (such as discretization error under insufficient grid resolution)

The feedback law in Eq. (6) inherently guarantees that the additional force term vanishes if the computational result converges to the experimental one. However, the feedback signal of the present hybrid tunnel intends to compensate the error of the numerical simulation due to the two-dimensionality and the insufficient grid resolution in order to obtain an accurate result for the relevant flow.

The above-mentioned feedback signal should be effective in reproducing the oscillation due to the Karman vortex shedding but not for the upstream boundary velocity. Therefore, the upstream uniform flow velocity U_0 of the real flow is also estimated from the pressure measurement, and is fed forward to the upstream boundary velocity U_b of the simulation.

From the Pitot tube law[11] the estimated upstream uniform flow velocity U_e is given by

$$U_e = K_e \sqrt{\frac{2P_m^*}{\rho}}, \tag{7}$$

where K_e is the velocity coefficient and P_m^* the dynamic pressure. In considering the characteristic of the Karman vortex that pressures on the both sides of the cylinder oscillate in opposite phases, the dynamic pressure P_m^* is estimated as

$$P_m^* = -\frac{P_{AS}^* + P_{BS}^*}{2} = P_S^* - \frac{P_A^* + P_B^*}{2}. \tag{8}$$

In order to remove the effect of the high-frequency component remaining in P_m^*, the first-order low-pass filter is applied to the upstream boundary velocity U_b as

$$T_c \frac{dU_b}{dt} + U_b = U_e, \tag{9}$$

where T_c represents the time constant.

Figure 4 shows a block diagram of the hybrid wind tunnel described above. Integration of numerical simulation and experimental measurement in the present hybrid wind tunnel implies the direct coupling of two methods through the feedback loop and the feedforward path. From the measurement and the computation of the differential pressures between the center of each side wall and that of the front wall, the feedback signals of the artificial forces f_A and f_B (chain line in Fig. 4), and the feedforward signal of the upstream boundary velocity U_b (broken line in Fig. 4) are defined. The parameters to be designed in the hybrid wind tunnel are the feedback gain K in Eq. (6), the velocity coefficient K_e in Eq. (7), and the time constant T_c in Eq. (9).

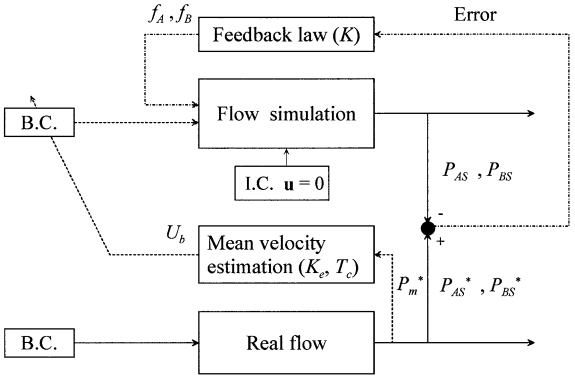

Fig. 4 Structure of the hybrid wind tunnel for the analysis of the flow with the Karman vortex street

3. Evaluation of the Hybrid Wind Tunnel

3.1 Evaluation at the monitoring point

The above-mentioned design parameters of the hybrid wind tunnel are so determined that the calculated velocity u at the monitoring point M $[(x,y,z) = (5D, 1.67D, 0)$, Fig. 2], where the velocity fluctuation due to the Karman vortex appears most clearly, best agrees with that of the experiment. In the followings, the validity of the hybrid wind tunnel is evaluated by comparing the result with those of the experiment and the ordinary numerical simulation.

3.1.1 Experiment Figure 5 (a) shows the experimental result for the differential pressure $P_{AS}{}^*$ in Eq. (4) (output signal of the experimental measurement), and the estimated dynamic pressure in Eq. (8) with opposite sign, $-P_m{}^*$. The differential pressure $P_{AS}{}^*$ shows nearly periodical oscillation with fluctuating amplitude due to the Karman vortex shedding. In the estimated dynamic pressure $P_m{}^*$, the main frequency component of the Karman vortex is removed, but there still retains high-frequency perturbation, which is suppressed through the low-pass filter in the estimation of the upstream boundary velocity in the hybrid

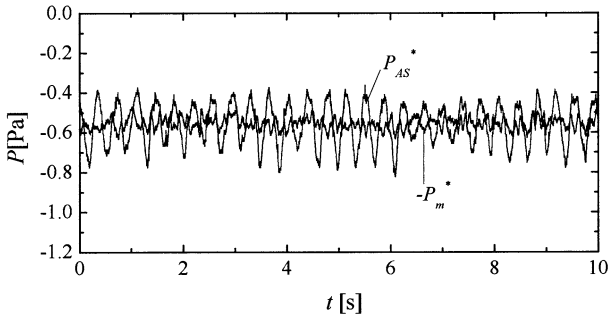

(a) Pressure at A on the cylinder wall and estimated dynamic pressure

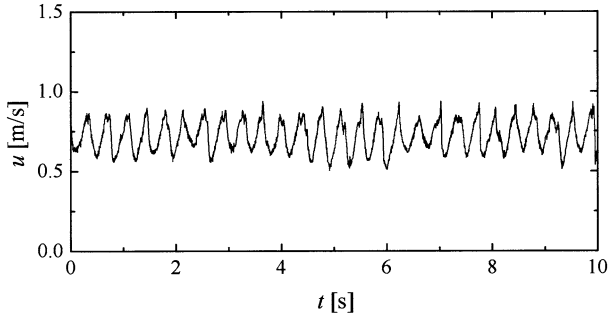

(b) Velocity at the monitoring point **M**

Fig. 5 Experimental result

wind tunnel. Figure 5 (b) depicts the velocity u measured with the LDV at the monitoring point M. It shows almost periodical oscillation with fluctuating amplitude synchronizing with the pressure variation.

3.1.2 Ordinary simulation Figure 6 shows the corresponding result of the ordinary numerical simulation. The upstream boundary velocity U_b is fixed to U_0, upstream uniform flow velocity of the experiment. A long transient state of 8 s corresponds to the formation of twin vortices before establishment of the Karman vortex shedding. In Fig. 6 (b), the amplitude of the steady oscillation in velocity u at the monitoring point **M** is much smaller than that of the experiment (Fig. 5 (b)). Quantitative comparison of the results including that of the hybrid wind tunnel will be discussed later with reference to Table 3. The numerical solution improves to some extent with the grid refinement, but the considerable amount of error in the frequency and the amplitude of the oscillation still remains in the grid-convergent solution for the present two-dimensional model[12]. Furthermore, the ordinary simulation is inherently incapable of reproducing the exact waveform of the real flow oscillation with irregular fluctuation since the exact initial and boundary conditions cannot be specified due to limited measurement data and unavoidable disturbances. The chaotic nature of the relevant flow may make the problem more difficult. A very slight difference in the initial condition increases exponentially in structurally unstable systems. The hybrid wind tunnel intends to reproduce the real flow by continuously supplying the information of the real flow to the numerical simulation.

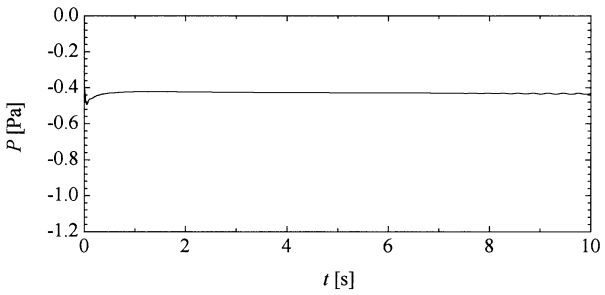

(a) Pressure at A on the cylinder wall

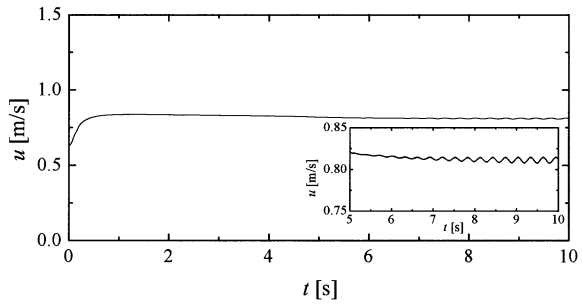

(b) Velocity at the monitoring point M

Fig. 6 Result of the ordinary simulation

3.1.3 Hybrid wind tunnel Since the present paper focuses on evaluating the accuracy of the hybrid wind tunnel, the computation in the hybrid wind tunnel is performed as the off-line process using the measurement data obtained in advance. Realization of real-time operation, which closely depends on the performance of the hardware for both the computation and transmission of data, is put aside for future study.

From calculations with variety of combinations of three parameters of the hybrid wind tunnel, we obtained the set of parameters that yields the best agreement with the experimental result for the velocity u at the monitoring point M as given in Table 2.

Figure 7 compares the result of the hybrid wind tunnel with that of the experiment. Figure 7 (a) shows the differential pressure between the center of the side wall and that of the front wall (output signal). The waveform of the pressure oscillation with the hybrid wind tunnel agrees well with that of the experiment except for a small bias. Comparison of the velocity u at the monitoring point M in Fig. 7 (b) reveals that the result of the hybrid wind tunnel precisely tracks the velocity variation of the experiment after the transient state in $t = 0 - 3$ s. As compared with the

Table 2 Parameter values of the hybrid wind tunnel determined from the velocity u at the monitoring point M

Feedback gain K	1.8
Velocity coefficient K_e	0.54
Time constant T_c	0.3 s

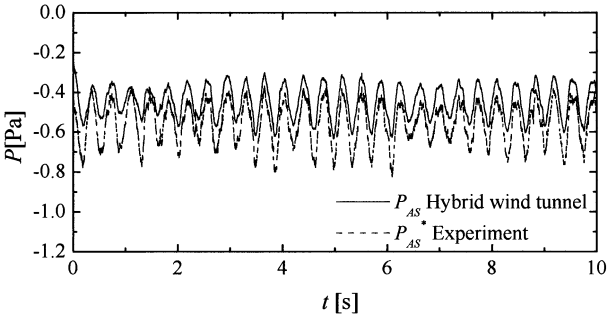

(a) Pressure at **A** on the cylinder wall

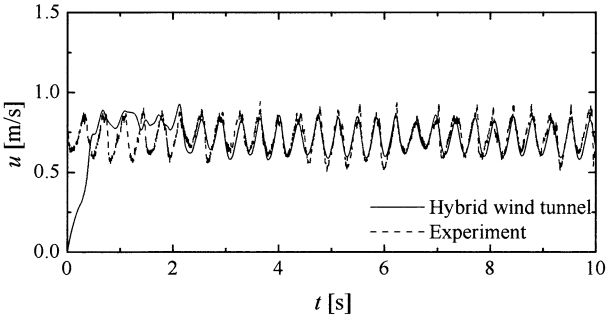

(b) Velocity at the monitoring point **M**

Fig. 7 Result of the hybrid wind tunnel compared with the experimental one

former result of the ordinary simulation (Fig. 6 (b)), the hybrid wind tunnel attains significant improvement in the reproducibility of the velocity u at the monitoring point. In addition, the transient state of the hybrid wind tunnel is shorter than that of the ordinary simulation.

Figure 8 shows the sensitivity of the result to each parameter. Figure 8 (a) compares the results for the feedback gain K in Eq. (6). As the gain K is decreased from the optimal value of 1.8, the oscillation amplitude decreases while the phase remains unchanged. The waveform with $K = 0.2$ completely differs from that of the experiment. Note that the ordinary numerical simulation shown in Fig. 6 (b) corresponds to the case of $K = 0$. As the feedback gain is increased from the optimal value, on the other hand, the amplitude of oscillation increases and the computation encounters instability at $K = 2.2$. To summarize these results, the rms error of the velocity u at the monitoring point is limited within 8% for the relatively wide range of $K = 1.2 - 2.0$, implying that the performance of the present hybrid wind tunnel is robust to the change of the gain K.

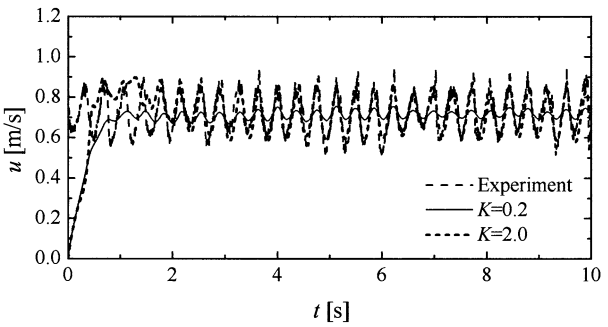

(a) Feedback gain K

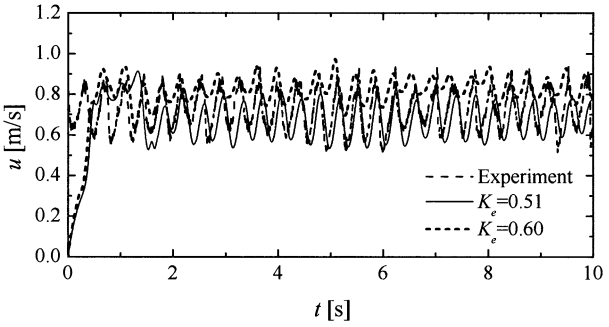

(b) Velocity coefficient K_e

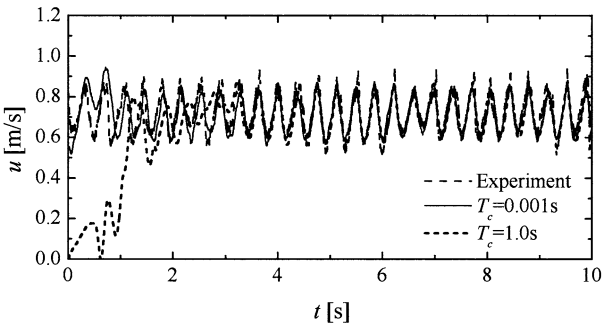

(c) Time constant T_c

Fig. 8 Effect of the parameters

Next, the results for the velocity coefficient K_e are compared in Fig. 8 (b). The mean value of the velocity u changes in accordance with K_e since the estimated upstream uniform flow velocity U_e is proportional to K_e in Eq. (7). The velocity coefficient K_e also influences the velocity oscillation pattern. The oscillation amplitude substantially decreases with slight increment of K_e. When K_e is decreased, on the other hand, its amplitude remains unchanged, but its phase shifts from that of the experiment. As the result, the rms error of the velocity remains within 10% for a rather narrow range of $K_e = 0.53 - 0.56$, implying that the performance of the present hybrid wind tunnel is sensitive to the change of the velocity coefficient K_e.

Finally, Fig. 8 (c) compares the results for the time constant T_c of the low-pass filter. The time constant influences the transient state but not the steady oscillation. As the time constant decreases, a high-frequency component intensifies in the upstream boundary velocity U_b, and the convergence property of the calculation is degraded. When T_c is set to 0.001 s, equal to the time step of the simulation, the calculation time for one time step is three times as in the case of $T_c = 1.0$ s. In consideration of both the calculation time and the transient time, the time constant T_c is determined as 0.3 s.

Table 3 summarizes the mean velocity u_{mean}, the rms of the velocity perturbation u'_{rms}, and its peak frequency obtained through FFT analysis. In order to remove the effect of the transient state, data is processed in $t = 10 - 30$ s. The results for the ordinary simulation and the hybrid wind tunnel are presented in terms of the ratio to experimental values. It is apparent that the hybrid wind tunnel gives far better agreement with the experiment than the ordinary simulation does.

Finally, Fig. 9 compares the results of FFT analysis for the velocity perturbation u' at the monitoring point **M** between the hybrid wind tunnel and the experiment. At the peak frequency (2.75 Hz), the amplitude obtained with the hybrid wind tunnel agrees well with that of the experiment (−0.5 dB), but in the high frequency domain (> 10 Hz), the amplitude for the hybrid wind tunnel exhibits a smaller value (< −13 dB).

Table 3 Comparison of the reproducibility in the velocity u at the monitoring point **M** between the ordinary simulation and the hybrid wind tunnel. Results are normalized with respect to the experimental values.

	u_{mean}	u'_{rms}	Peak frequency
Experiment	1	1	1
Ordinary simulation	1.13	0.03	1.20
Hybrid wind tunnel	0.99	0.89	1.00

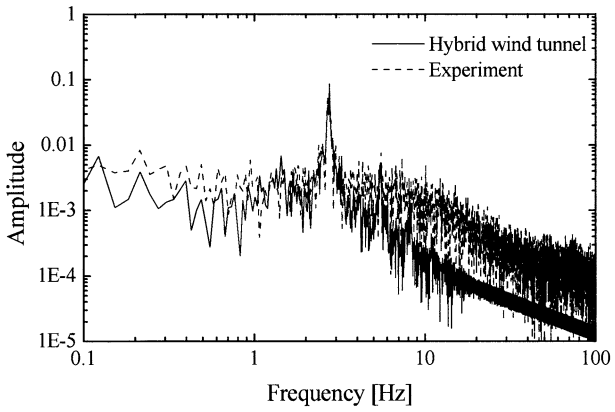

Fig. 9 FFT analysis for the velocity perturbation u' at the monitoring point **M**

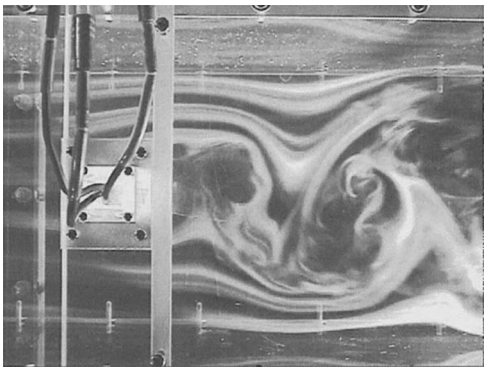

(a) Experiment

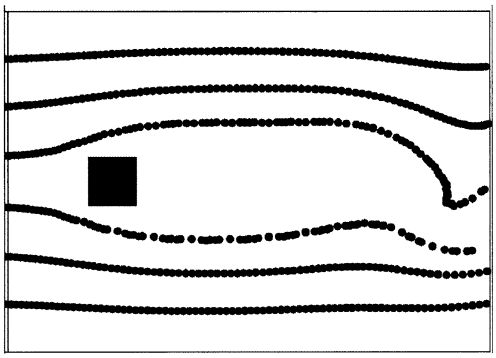

(b) Ordinary simulation

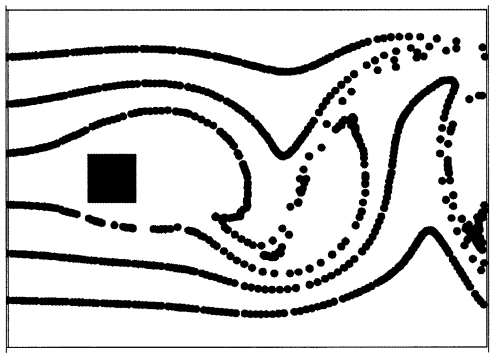

(c) Hybrid wind tunnel

Fig. 10 Streak lines ($t = 17.9$ s)

3.2 Evaluation over the flow domain

In this section, the reproducibility of the hybrid wind tunnel is investigated over the whole flow domain.

First, Fig. 10 compares the streak lines at the same instant among the experiment, the ordinary simulation, and the hybrid wind tunnel. Streak lines in the experiment represent the typical flow pattern of the Karman vortex street (Fig. 10 (a)). The ordinary numerical simulation in Fig. 10 (b) shows a completely different flow pattern from that of the experiment. As shown in Fig. 10 (c), the hybrid wind tunnel yields a very similar flow pattern to that of the experiment, including the phase of the oscillation.

In the following discussion, the velocity field is compared among the experiment, the ordinary simulation, and the hybrid wind tunnel. Measurement of the velocity u was first conducted with the LDV at 413 measurement points in the flow domain of $0 \le x \le 18D$ (see Fig. 2), while the differential pressure between the center of each side wall and that of the front wall of the square cylinder was measured. Then the flow analysis was carried out with the hybrid wind tunnel using 413 pressure measurement data. The velocity field of u was compared in terms of the mean velocity u_{mean}, the rms of velocity perturbation u'_{rms}, and the rms of the difference of the velocity u. As in the previous section, the data was processed in $t = 10-$

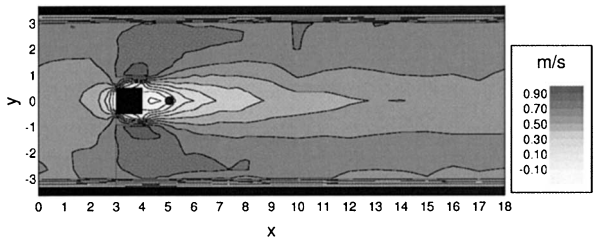

(a) Experiment

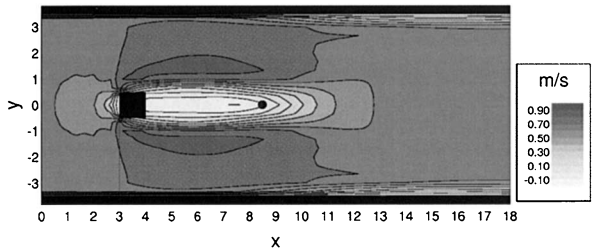

(b) Ordinary simulation

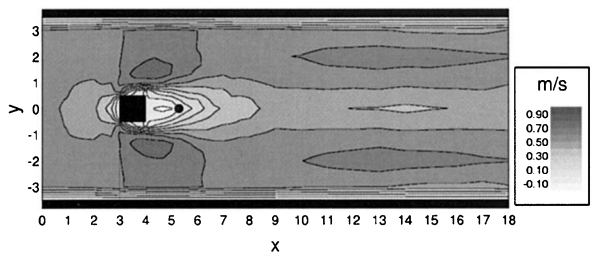

(c) Hybrid wind tunnel

Fig. 11 Distribution of the mean velocity u_{mean}

30 s in order to remove the effect of the transient state. Since the laser beam is obstructed by the cylinder in the region $3D \le x \le 4D$ and $-0.5D \le y \le 3.5D$, the experimental data were compensated with those measured at the position symmetric about the x-axis. Experimental values are linearly interpolated at the computational grid points in the region where the measurement was performed sparsely ($x = D$ and $8D \le x \le 18D$). In the following figures, coordinates are normalized with the width of the cylinder for simplicity.

Figure 11 compares contour lines of the mean velocity u_{mean}. Note that the value at each point corresponds to one of 413 different measurements for the results of the experiment and the hybrid wind tunnel. Contour level increases from white to black. The symbol • denotes the contour line at $u_{mean} = 0$ in the wake. In comparison with the experiment (Fig. 11 (a)), the recirculation region behind the cylinder in the ordinary simulation (Fig. 11 (b)) is considerably stretched, whereas that of the hybrid wind tunnel (Fig. 11 (c)) is very similar to that of the experiment. The x-position of the minimum velocity is $x = 4.3$, 7.7, and 4.7 for the experiment, the ordinary simulation, and the hybrid wind tunnel, respectively.

Contour lines of the velocity perturbation u'_{rms} are compared in Fig. 12. In the experimental result in Fig. 12 (a), large velocity perturbation appears near the downstream corners of the cylinder because of vortex shedding, which gradually decreases downstream almost spreading out in the region $x > 10$. The distribution with the ordinary simulation in Fig. 12 (b) is completely different from that of the experiment. Large velocity perturbation resulting from the Karman vortex occurs far downstream of the cylinder around $x = 10$. The result of the hybrid wind tunnel in Fig. 12 (c) shows a good agreement with that of the experiment near behind the cylinder. However, in far downstream region with $x > 10$, there exists non-uniformity in velocity perturbation in contradiction with the experiment. This discrepancy is probably ascribed to insufficient mixing in the two-dimensional flow model.

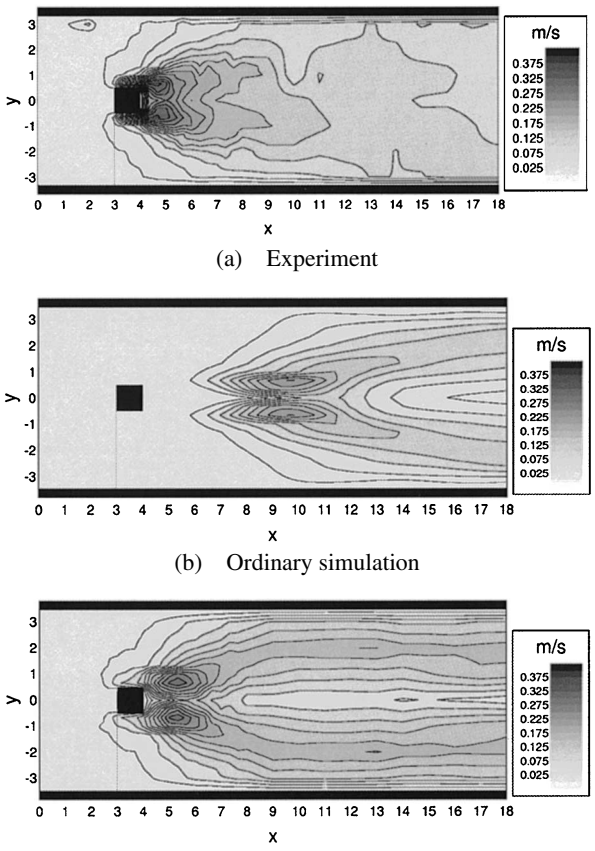

(a) Experiment

(b) Ordinary simulation

(c) Hybrid wind tunnel

Fig. 12 Distribution of the velocity perturbation u'_{rms}

In the followings, the error of the hybrid wind tunnel is quantified over the all computational grid points. First, the error in the mean velocity u_{mean} and the velocity perturbation u'_{rms} are separately evaluated in Figs. 13 (a) and (b), and then the rms error in the velocity u is obtained in Fig. 13 (c). All the values shown in these figures are normalized with respect to the upstream uniform flow velocity U_0. Note that values in Figs. 13 (a) and (b) are positive or negative, and a positive value means that the hybrid wind tunnel gives a larger value than the experiment. In Fig. 13 (a) the maximum error of the mean velocity with the hybrid wind tunnel corresponds to the smallest differ-

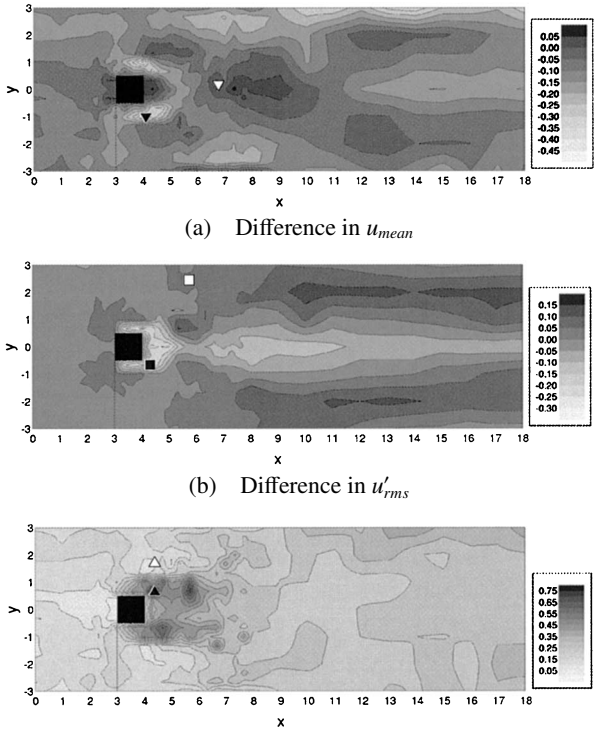

(a) Difference in u_{mean}

(b) Difference in u'_{rms}

(c) Rms error in the velocity u

Fig. 13 Difference of the hybrid wind tunnel from the experiment

ence of −0.42 at the position near the cylinder denoted by ▼, and the minimum error of 0.00 is found at some distance behind the cylinder at the position denoted by ▽. Note that the position of the maximum or minimum error is chosen from 60×21 computational grid points. The mean value of the difference in u_{mean} evaluated over the whole grid points is −0.12. In Fig. 13 (b) the maximum error of the rms value of the velocity perturbation corresponding to the smallest difference of −0.28 is found at the position with ■ near the position of the maximum error of the mean velocity mentioned above, the minimum error of 0.00 at the position with □. The mean value of the difference in u'_{rms} evaluated over the whole grid points is 0.01. The rms error of the hybrid wind tunnel in evaluating the velocity u is plotted in Fig. 13 (c). The maximum error of 0.74 is found at the position with ▲ that is the mirror point of the maximum error of the velocity perturbation, and the minimum error of 0.07 at the position

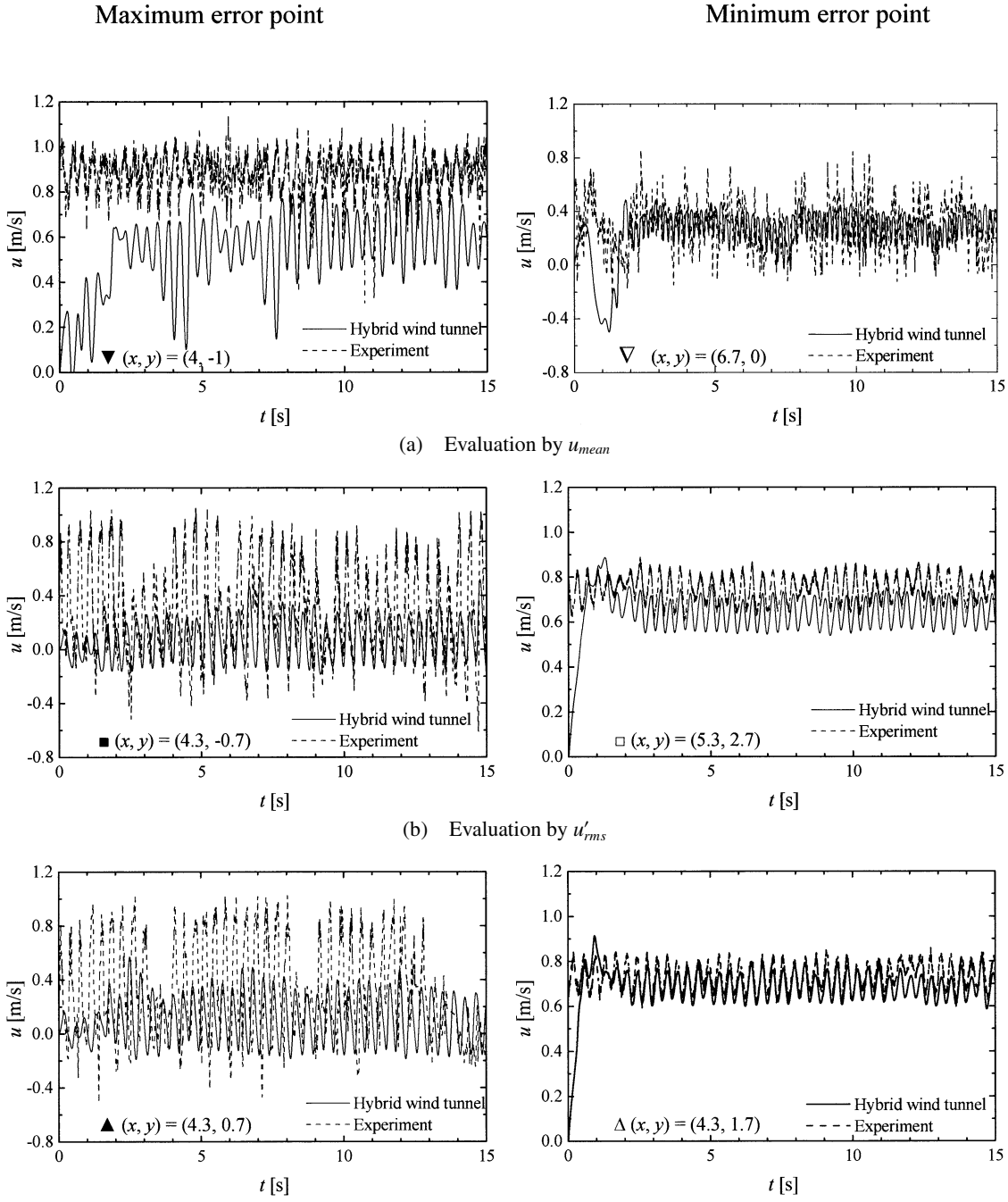

(a) Evaluation by u_{mean}

(b) Evaluation by u'_{rms}

(c) Evaluation by rms error in the velocity u

Fig. 14 Comparison of u at the characteristic points (the left-hand side figures correspond to the maximum error points and the right-hand side to the minimum)

with △ that is close to the monitoring point **M**. The mean value of the rms error of the velocity u evaluated over the whole grid points is 0.23. Note that the maximum error occurs near the downstream corner of the cylinder for all three characteristic values. In order to improve the accuracy of the hybrid wind tunnel in the near region behind the cylinder, improvement in measurement, computation, and feedback should be considered. These are, for example, additional output signal, finer computational grid, and additional feedback signal.

Finally, Fig. 14 compares the velocity variation between the hybrid wind tunnel and the experiment at the maximum and the minimum error points for three characteristic values. The left- and right hand side figures correspond to the results at the maximum and minimum error points, respectively. Note that the maximum error points locate close together near behind the cylinder, whereas the minimum error points disperse in a wide region. Investigation over the all grid points has shown that the hybrid wind tunnel has good reproducibility of the velocity in most of the domain (including ○, △, ▽, and □ in Fig. 2) except for the region near behind the cylinder (including ▲, ▼, and ■).

In this section it has been confirmed that the hybrid wind tunnel, which is designed using the velocity u at the monitoring point M, reproduces the real flow in most of the flow domain.

4. Conclusions

In this paper we have developed a new flow analysis system, namely the hybrid wind tunnel, which integrates the experimental measurement with a wind tunnel and the corresponding numerical simulation with a computer. Analysis has been performed for the fundamental flow with the Karman vortex street in a wake of a square cylinder. A specific feature of the hybrid wind tunnel is existence of the feedback signal to compensate the error in the pressure on the side walls of the cylinder and the feed-forward signal to adjust the upstream velocity boundary condition. Investigation is focused on evaluating the hybrid wind tunnel as a flow analysis methodology with respect to the ordinary simulation or the experiment. As compared with the ordinary simulation, the hybrid wind tunnel substantially improves the accuracy and the efficiency in the analysis of the relevant flow. Especially, the oscillation of the flow with the hybrid wind tunnel exactly synchronizes with that of the experiment, while that with the ordinary simulation never behave like that. In comparison with the experiment, the hybrid wind tunnel provides more detailed information of the flow than the experiment does.

The mathematical model in the present hybrid wind tunnel assumes two-dimensional model for simplicity. Although the result is satisfactory in comparison with the ordinary simulation, three-dimensional analysis should be crucial for further investigation including the grid convergence property. In addition, present analysis has been performed using off-line measurement in order to evaluate the accuracy of the hybrid wind tunnel. Realization of the analysis system capable of the real-time operation remains for the future work. As to the feedback and/or feedforward strategy, the present paper has dealt with only a possible simplest case. Further investigation for this problem should be the key issue to generalize the hybrid wind tunnel as the flow analysis tool.

Acknowledgements

The authors express their sincere thanks to Technicians, T. Hamaya, T. Watanabe, Y. Fushimi, and K. Asano of the Institute of Fluid Science, Tohoku University for construction of the experimental apparatus, and to graduate student S. Takeda for his patient experimental measurement. The authors gratefully acknowledge support received from a Grant-in-aid for Scientific Research (#10650157,11555053). The calculations were performed using ORIGIN 2000 in the Advanced Fluid Information Research Center, Institute of Fluid Science, Tohoku University.

References

(1) Hayase, T. and Hayashi, S., State Estimator of Flow as an Integrated Computational Method with the Feedback of Online Experimental Measurement, ASME Journal of Fluids Engineering, Vol.119 (1997), pp.814–822.

(2) Lee, B.E., The Effect of Turbulence on the Surface Pressure Field of a Square Prism, Journal of Fluid Mechanics, Vol.69, Part 2 (1975), pp.263–282.

(3) Lyn, D.A., Einav, S., Rodi, W. and Park, J.-H., A Laser-Doppler Velocimetry Study of Ensemble-Averaged Characteristics of the Turbulent Near Wake of a Square Cylinder, Journal of Fluid Mechanics, Vol.304 (1995), pp.285–319.

(4) Rodi, W., Ferziger, J.H., Breuer, M. and Pourquié, M., Status of Large Eddy Simulation: Results of a Workshop, ASME Journal of Fluids Engineering, Vol.119 (1997), pp.248–262.

(5) Bearman, P.W. and Obasaju, E.D., An Experimental Study of Pressure Fluctuations on Fixed and Oscillating Square-Section Cylinders, Journal of Fluid Mechanics, Vol.119 (1982), pp.297–321.

(6) Sakamoto, H., Tan, K., Takeuchi, N. and Haniu, H., Suppression of Fluid Forces Acting on a Square Prism by Passive Control, ASME Journal of Fluids Engineering, Vol.119 (1997), pp.506–511.

(7) Roussopoulos, K., Feedback Control of Vortex Shedding at Low Reynolds Numbers, Journal of Fluid Mechanics, Vol.248 (1993), pp.267–296.

(8) Patankar, S.V., Numerical Heat Transfer and Fluid Flow, (1980), Hemisphere, Washington, DC/New York.

(9) Hayase, T., Humphrey, J.A.C. and Greif, R., A Con-

sistently Formulated QUICK Scheme for Fast and Stable Convergence Using Finite-Volume Iterative Calculation Procedures, Journal of Computational Physics, Vol.98, No.1 (1992), pp.108–118.

(10) Hayase, T., Monotonic Convergence Property of Turbulent Flow Solution with Central Difference and QUICK Schemes, ASME Journal of Fluids Engineering, Vol.121 (1999), pp.351–358.

(11) Rosenhead, L. (ed.), Laminar Boundary Layers, (1963), p.593, Oxford University Press.

(12) Hayase, T., Nisugi, K. and Shirai, A., Numerical Realization of Flow Field by Integrating Computation and Measurement, Proceedings of Fifth World Congress on Computational Mechanics (WCCM V), Paper-ID: 81524, (2002), pp.1–12.